ACS Catalysis

pubs.acs.org/acscatalysis

Research Article

Electrochemical CO_2 Reduction over Metal-/Nitrogen-Doped Graphene Single-Atom Catalysts Modeled Using the Grand-Canonical Density Functional Theory

Paige Brimley,[∇] Hussain Almajed,[∇] Yousef Alsunni, Abdulaziz W. Alherz,* Zachary J. L. Bare, Wilson A. Smith, and Charles B. Musgrave*

Cite This: *ACS Catal.* 2022, 12, 10161−10171

Read Online

ACCESS | Metrics & More | Article Recommendations | Supporting Information

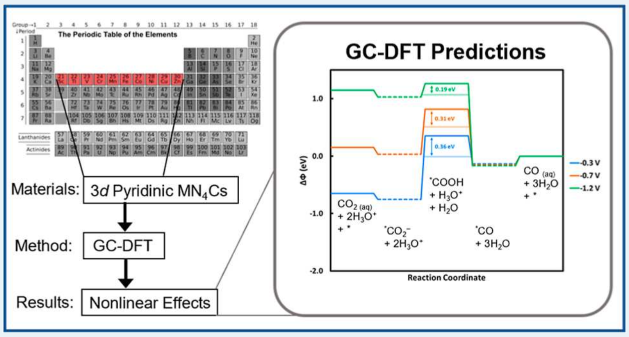

ABSTRACT: Renewably driven, electrochemical conversion of carbon dioxide into value-added products is expected to be a critical tool in global decarbonization. However, theoretical studies based on the computational hydrogen electrode largely ignore the nonlinear effects of the applied potential on the calculated results, leading to inaccurate predictions of catalytic behavior or mechanistic pathways. Here, we use grand canonical density functional theory (GC-DFT) to model electrochemical CO_2 reduction (CO_2R) over metal- and nitrogen-doped graphene catalysts (MNCs) and explicitly include the effects of the applied potential. We used GC-DFT to compute the CO_2 to CO reaction intermediate energies at −0.3, −0.7, and −1.2 V_{SHE} catalyzed by MNCs each doped with 1 of the 10 3d block metals coordinated by four pyridinic nitrogen atoms. Our results predict that Sc-, Ti-, Co-, Cu-, and Zn-N_4Cs effectively catalyze CO_2R at moderate to large reducing potentials (−0.7 to −1.2 V_{SHE}). ZnN_4C is a particularly promising electrocatalyst for CO_2R to CO both at low and moderate applied potentials based on our thermodynamic analysis. Our findings also explain the observed pH independence of CO production over FeN_4C and predict that the rate-determining step of CO_2R over FeN_4C is not $^*CO_2^-$ formation but rather *CO desorption. Additionally, the GC-DFT-computed density of states analysis illustrates how the electronic states of MNCs and adsorbates change non-uniformly with applied potential, resulting in a significantly increased $^*CO_2^-$ stability relative to other intermediates and demonstrating that the formation of the adsorbed $^*CO_2^-$ anion is critical to CO_2R activation. This work demonstrates how GC-DFT paves the way for physically realistic and accurate theoretical simulations of reacting electrochemical systems.

KEYWORDS: *single-atom catalysts, electrochemistry, grand canonical density functional theory, DFT calculations, surface chemistry, CO_2 reduction*

■ INTRODUCTION

Excess atmospheric carbon dioxide (CO_2) is a major contributor to global warming, yet CO_2 is emitted from nearly every modern industrial process. As an alternative to atmospheric release or sequestration, electrochemical CO_2 reduction (CO_2R) can convert captured CO_2 into value-added products.[1] CO_2R on pure metal electrodes, such as copper, requires large overpotentials to drive CO_2 conversion and competes with the hydrogen evolution reaction (HER) at all potentials.[2−4] Gold and silver, which are arguably the best electrocatalysts for CO_2R to CO, are prohibitively expensive for large-scale applications.[5,6]

An emergent class of electrocatalysts for CO_2R is two-dimensional metal-nitrogen-doped carbon (MNC) materials where a metal center, usually a first−row transition metal, is bound to the nitrogen atoms of N-doped graphene.[7] The metal atoms of MNCs are assumed to be the catalytically active sites and are analogous to those of naturally occurring porphyrin complexes, such as chlorophyll and heme.[8] MNCs are an attractive alternative to bulk metal catalysts as they have near maximal metal atom utilization, are highly selective for reducing CO_2 to CO at moderate potentials, and are composed of relatively earth abundant and inexpensive elements.[2,9] Experimental studies have demonstrated the high selectivity of CO_2R catalyzed by several MNCs toward CO with MnN_xC (where typically $x \in [1, 2, 3, 4]$) achieving a Faradaic efficiency (FE) of up to 80%, FeN_xC and NiN_xC

Received: April 14, 2022
Revised: July 5, 2022
Published: August 4, 2022

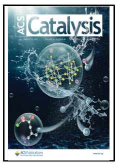

ACS Publications

https://doi.org/10.1021/acscatal.2c01832

reaching FEs over 85%, and ZnN_xC attaining a FE of up to 95%.[10−17]

While MNCs have exhibited significant promise for CO_2R, many questions persist about the nature of their active sites and activation mechanisms. MNC synthesis generates a range of dispersed atomic structures that likely contribute unequally to the catalytic activity and promote different catalytic mechanisms. The MN_4C sites are observed to have a square-planar geometry, where the pyridinic coordination of the metal by four nitrogen atoms (Figure 1) is reported to be the most stable, although recent work has strongly suggested that a lower nitrogen coordination might increase the catalytic activity of CO_2R over some MNCs.[17−20] Ideally, future materials for CO_2R catalysis would synthetically select for the most active site; however, experimental determination of the CO_2R active site remains a daunting challenge even with state-of-the-art electrochemical characterization techniques.[21] In contrast, computational models can be used to directly investigate the reactivity of hypothetical reactive sites and mechanisms as they explicitly model reactions in atomic detail. For this work, we developed atomistic models that describe the CO_2R activity of the pyridinic MN_4C site because it is the most stable MNC configuration, the most widely reported active site for MNC-catalyzed CO_2R to CO, and highly selective toward CO production through the suppression of the HER.[22−24]

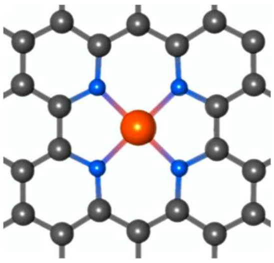

Figure 1. Structure of an MN_4C catalyst where a 3d-transition metal atom (orange) is coordinated to four pyridinic nitrogen atoms (blue) doped into a graphene lattice (gray).

The number of electrons at a reactive site of an electrochemical interface depends on the applied potential, catalyst, solvent, electrolyte, and state along the reaction potential energy surface. However, modeling the electrified catalyst−solvent interface with traditional density functional theory (DFT) is not physically realistic because it is a canonical, fixed-electron number approach (which we refer to as unbiased calculations).[25] For over a decade, the simple and elegant computational hydrogen electrode (CHE) model has served as the workhorse for estimating the effects of applied potential on electrocatalytic processes.[26] However, the tradeoff for its ease of application is that it does not explicitly include the electrode potential in the quantum chemical model and instead adjusts for the potential through post-minimization algebraic corrections. DFT has recently been extended to grand-canonical DFT (GC-DFT), which naturally accounts for the applied potential by self-consistently varying the number of electrons in the system such that its Fermi level is in equilibrium with the applied external potential.[27,28]

Additionally, the constraint of charge neutrality requires the use of a solvent model in GC-DFT calculations to account for the variable number of electrons.[29] DFT has traditionally been used with a catalyst−vacuum interface model to describe catalyst−electrolyte interfaces;[12,30−32] however, several researchers have approximated the solvation energies of intermediates and added them as empirical correction values,[31,33−35] which provided more accurate results than model vacuum calculations. More recently, solvation effects have been modeled with a polarizable continuum and/or explicit solvent molecules,[36] both producing moderately more accurate energies than previous approaches. Our group has previously shown, and further demonstrates in this work, that surface and adsorbate geometries can vary significantly with applied potential and solvent model, resulting in Helmholtz free energies and a projected density of states (PDOS) that change non-linearly with bias, which indicates that orbital mixing is significantly affected by the local electric field.[25] The results of these works have shown that GC-DFT is able to capture CO_2R behavior that the CHE + an implicit solvent model cannot, both for well-studied systems (such as Cu and Ag) and for novel systems. Thus, the major advantage of GC-DFT is its ability to self-consistently account for both the interdependent effects of the solvent and the applied bias.

In this contribution, we report the results of applying GC-DFT to the electrocatalytic reduction of CO_2 to CO over pyridinic MN_4Cs formed by the 10 3d-block metals. We also provide a fundamental description of the effects of the applied potential on the electronic structure of CO_2 adsorbed on pyridinic MN_4C sites through PDOS analysis. Although different nitrogen functionalities (pyridinic, pyrrolic, etc.), defect sites, electrolyte choice, and the sensitivity of activation barriers to the potential affect the reactivity of active sites toward CO_2R, they are beyond the scope of the present study. To the best of our knowledge, this is the first study to fully implement GC-DFT to comprehensively compare the thermodynamics of the 10 3d-block MN_4Cs in the pyridinic configuration for catalyzing the electrochemical CO_2R reaction. This work also illustrates how GC-DFT is a viable new approach for accurately and realistically modeling electrocatalytic systems.

METHODS

Method Justification. Most DFT studies of electrochemical processes calculate the reaction energetics using conventional DFT corresponding to an unbiased, neutral charge system. Such studies typically treat solvation using implicit or explicit models and account for applied bias effects using empirical corrections from the CHE.[7,9,12,28,37−39] The CHE approach adjusts the DFT-computed energies of adsorbed species by a constant value of $ne\varphi$, where φ is the potential and n is the formal number of electrons transferred by the redox process, and is restricted to only estimating energies of intermediates that are formed via a proton-coupled electron transfer (PCET) mechanism. Furthermore, the CHE model neglects the direct effects of the applied bias on the interface, including the change in the electronic structure caused by the addition or removal of electrons, the non-integer changes in transferred electrons, the change in the electronic states because of polarization by the applied electric field, and the change in the geometry of the reacting species at different applied biases.[25]

To describe the interactions between adsorbates and the electrified interface, the grand free energy can be computed within the grand canonical ensemble formalism in which the temperature, volume, and electron chemical potential (Fermi energy) are fixed. A constant electron chemical potential dictates that the number of electrons is self-consistently varied and thus the GC ensemble is a more natural ensemble with which to calculate properties of electrochemical systems.[25,28] GC-DFT is an ab initio approach that computes the grand free energy by self-consistently solving the Kohn−Sham equations while varying the number of electrons at the electrode to maintain a constant Fermi level that corresponds to the applied potential. Although GC-DFT calculations are more computationally demanding, when coupled with proper solvation models, they more accurately describe states along the reaction coordinate as a function of the potential which, in many cases, differ considerably from the results of conventional DFT calculations.[25,28,29,40] For a more theoretical description of GC-DFT and its application to electrochemistry, the reader is referred to Sundararaman et al.'s work.[28]

Computational Details. The intermediate geometries along the CO_2R reaction pathway on MN_4Cs were optimized using GC-DFT as implemented within Sundararaman et al.'s open-source JDFTx code.[27] MN_4C reactive sites were modeled with a 12 Å × 12 Å × 22 Å 2-dimensional supercell comprising 44 carbon atoms, 4 pyridinic nitrogen atoms, and 1 3d metal center as well as implicit solvent that fills the ~20 Å separation between MN_4C sheets. A planewave expansion with a 544 eV (20 Hartree) energy cutoff and a 3 × 3 × 1 gamma-centered *k*-point grid were confirmed to provide good approximations to the asymptotic energy and *k*-point limits, respectively. Geometry optimizations were performed for all adsorbates until the total energies and forces were converged to within 10^{-6} Ht/cell and 10^{-4} Ht/Bohr, respectively. All GC-DFT calculations were performed using the generalized gradient approximation Perdew−Burke−Ernzerhof (GGA-PBE) exchange correlation functional combined with Grimme's DFT-D3 van der Waals correction and the GBRV pseudopotentials.[41,42] GGA-PBE was selected because of its high computational speed and relatively accurate prediction of free energies of heterogeneous catalysts. The DFT-D3 correction was chosen due to its structure dependence for calculating van der Waals interactions and its high accuracy in correcting for them. To describe the solvent, we chose the charge-asymmetric nonlocally determined local-electric (CANDLE) continuum solvation model due to its accurate description of polar solvents and their interactions with charged surfaces.[40] GC-DFT maintains charge neutrality of the periodic unit cell as the electron number changes with φ by introducing a compensating number of counterions in the electrolyte that distribute themselves to minimize the grand free energy.[27] One limitation of the CANDLE model is that it neglects ionic size effects on the reaction energetics, which have been shown to significantly alter catalytic activity for CO_2R.[43−45] However, the effects of cation size on the CO_2R reaction are beyond the scope of this study. A more detailed description of GC-DFT, energy calculations, and the solvation settings used in this study are provided in the Supporting Information.

RESULTS AND DISCUSSION

Several studies have suggested that a PCET is not involved in the rate-determining step (RDS) of CO_2R over MNCs or their molecular analogues.[13,37,46,47] Therefore, we evaluated a mechanism that proceeds through a decoupled-proton-electron-transfer (DPET) pathway as described by eqs 1−4

$$CO_{2(aq)} + {}^{*} + e^{-} \rightarrow {}^{*}CO_2^{-} \tag{1}$$

$$^{*}CO_2^{-} + H^{+}_{(aq)} \rightarrow {}^{*}COOH \tag{2}$$

$$^{*}COOH + H^{+}_{(aq)} + e^{-} \rightarrow {}^{*}CO + H_2O_{(l)} \tag{3}$$

$$^{*}CO \rightarrow CO_{(aq)} + {}^{*} \tag{4}$$

The asterisk (*) indicates an open MN_4C adsorption site. Note that only the second and third steps involve a proton transfer. Figure 2 shows representative intermediate structures along the CO_2R reaction coordinate. The grand free energies of these intermediates were computed at applied potentials of φ = −0.3, −0.7, and −1.2 V versus the standard hydrogen electrode (herein referred to as V_{SHE}) and are plotted in Figures 3−5. Transition state calculations are not performed in this study due to their significant computational cost within the GC-DFT approach. To connect the thermodynamics of our study with kinetics, we set a grand free energy threshold of 0.7 eV at which all catalysts with specific reaction steps more endergonic than this threshold were deemed too sluggish on lab time scales to be kinetically viable at 298 K. We note that this criterion is a necessary but insufficient condition for a mechanism to be kinetically active as the rate of a reaction path may be impractically slow because of transition states that lie too high in energy or less often because the activation entropy of the RDS is too low.

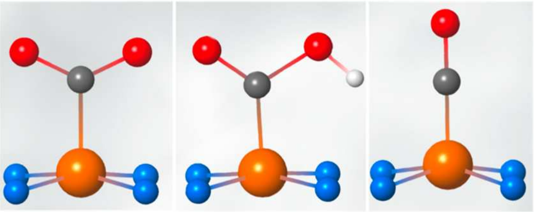

Figure 2. Geometries of CO_2R intermediates. The metal, carbon, nitrogen, oxygen, and hydrogen atoms are represented by orange, gray, blue, red, and white spheres, respectively.

Our GC-DFT results show that CO_2 does not adsorb chemically to a few 3d MN_4C catalysts at the metal site at various applied potentials. In the cases of NiN_4C and CuN_4C at all potentials as well as ZnN_4C at −0.3 V_{SHE} and −0.7 V_{SHE}, the first step of the mechanism involves a PCET, where aqueous CO_2 reacts with a proton-electron couple to form an adsorbed COOH. Note that this mechanism (i.e., PCET mechanism) is different from the one shown above (i.e., DPET mechanism). We discuss these cases below and provide more detail in the Supporting Information.

The grand free energies of the CO_2R reaction on all 10 pyridinic MN_4C systems are shown in Figures 3−5. A comparison of the GC-DFT calculated reaction coordinates and CHE calculated reaction coordinates are shown in Supporting Information, Figures S6−S8. All grand free energies were referenced to the product state, $CO_{(aq)}$ + $3H_2O_{(aq)}$ + *. This choice makes the energies of the product states for each system 0.0 eV at all biases, and the energies of the preceding states, including the reactants ($CO_{2(aq)}$ + $2H_3O^{+}_{(aq)}$ + *), all potential-dependent. However, the choice of the reference as either the reactant or product states is arbitrary as both reactants and products consist of solvated species and an open MN_4C site. Thus, the endergonicity or exergonicity of each reaction step and of the overall reaction is the same with either convention. We choose the products as

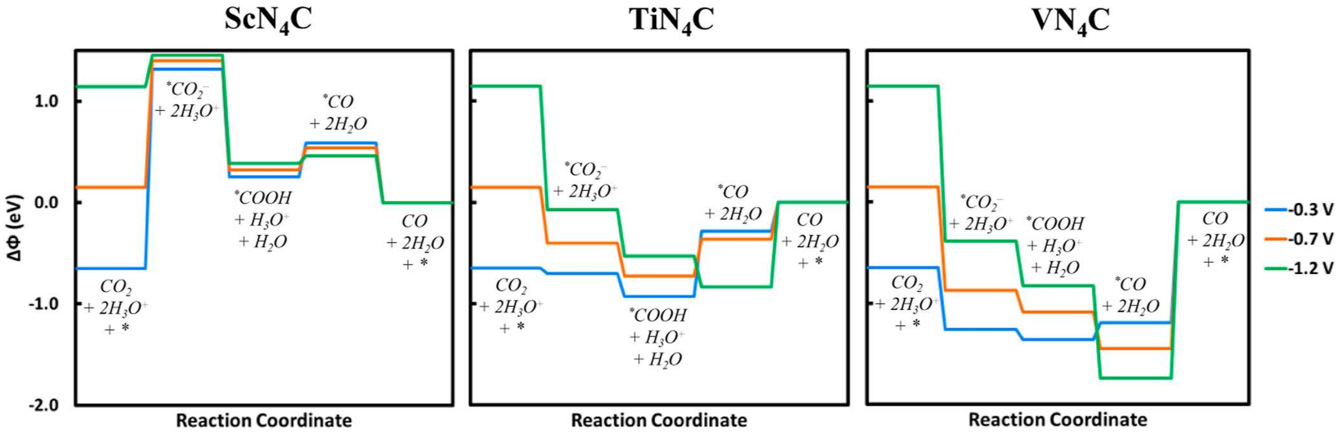

Figure 3. CO_2R reaction coordinate diagrams for Sc-, V-, and TiN_4C. Reaction grand free energies computed for applied reducing potentials of $\varphi = -0.3\ V_{SHE}$ (blue), $-0.7\ V_{SHE}$ (orange), and $-1.2\ V_{SHE}$ (green). Note that the nonlinearity of energy changes with applied potential is common across all three catalysts.

the reference state to follow a conventional workflow as our products consist of neutral molecules and are hence unaffected by applied external bias, assuming the operating conditions are between the molecules' oxidation and reduction potentials.

The GC-DFT computed trends in the grand free energies with applied potential are unique to the adsorbed intermediate and transition metal of the MN_4C. GC-DFT predicts that the energies of the reactant state, $CO_{2(aq)} + 2H_3O_{(aq)}^+ + *$, change more rapidly with φ than those of adsorbed CO_2 on all 10 MN_4Cs. This indicates that the CO_2 adsorption step is critical in activating CO_2R, despite commonly being ignored in various conventional DFT studies.[18,19,31,48,49] In this section, we divide our analysis into CO_2R over MN_4Cs composed of early, middle, and late 3d-block metals. We first discuss early 3d metal MN_4Cs.

CO_2R on Early 3d Metal MN_4Cs. There is a dearth of computational and experimental CO_2R studies of early 3d metals as dopants in single-atom catalysts because they are believed to be strong *OH and *CHO binders,[7,50] which limit their selectivity toward CO production. Figure 3 shows the reaction coordinate diagrams for CO_2R on ScN_4C, TiN_4C, and VN_4C at three reducing potentials computed using GC-DFT. The computed reaction energetics reported in these diagrams show that the shifts in the intermediate energies are significant and non-linear, in contrast to the predictions of the CHE model. They also show that adsorbed CO_2R intermediates become more stable as the atomic number of the metal center increases, and that metal centers with higher atomic numbers have more favorable bonding interactions with CO_2R intermediates. This is consistent with the order of M−CO_2, M−COOH, and M−CO bond lengths that decrease in the following order: Sc−R > Ti−R > V−R for the early 3d MN_4Cs (see the Supporting Information for details). The distinct bonding interactions between the intermediates and different metal centers also results in these three MNCs having different RDSs based on their relative intermediate energies. For instance, at $-0.3\ V_{SHE}$, CO_2 adsorption is rate limiting on ScN_4C, *COOH protonation is rate limiting on TiN_4C, and *CO desorption is rate limiting on VN_4C. On ScN_4C, the intermediate energies are insensitive to applied potential, but the reactants, $CO_{2(aq)} + 2H_3O_{(aq)}^+$, become more unstable relative to $*CO_2^-$ at more reducing biases. Thus, GC-DFT predicts that more reducing biases lower the free energy of the RDS of CO_2 adsorption on ScN_4C to enable faster kinetics. In contrast, the RDS on TiN_4C shifts from *COOH protonation to *CO desorption at more reducing biases, whereas on VN_4C, *CO desorption is sluggish and rate limiting at all biases and becomes more prohibitive at more reducing potentials. We discuss the *CO desorption energy trends in more detail for the rest of the MN_4Cs below to highlight its importance in predicting CO_2R performance over all 10 pyridinic 3d-MN_4Cs using GC-DFT.

GC-DFT predicts that $*CO_2^-$ is not thermodynamically stable on ScN_4C relative to $CO_{2(aq)}$ at biases less reducing than $-1.2\ V_{SHE}$. This suggests that $*CO_2^-$ is a short-lived species that is stabilized by a proton transfer to form *COOH. Alternatively, *COOH more likely forms through a PCET mechanism with $CO_{2(aq)}$ at the electrified interface that avoids the high energy $*CO_2^-$ intermediate. As mentioned above, the energy of formation of *COOH from aqueous CO_2 on ScN_4C changes significantly as we sweep the potential from −0.3 to $-1.2\ V_{SHE}$. At $-0.3\ V_{SHE}$, the required thermodynamic energy to form *COOH is +0.90 eV. This difference decreases to +0.17 and −0.76 eV at −0.7 and $-1.2\ V_{SHE}$, respectively, indicating a thermodynamically more facile pathway for *COOH formation at more cathodic potentials. Based on our thermodynamic criteria to assess CO_2R capability, ScN_4C would be able to reduce CO_2 to CO slowly at $-0.7\ V_{SHE}$, but more rapidly at $-1.2\ V_{SHE}$.

CO_2R on Middle 3d Metal MN_4Cs. CO_2R catalysis by Cr-, Mn-, Fe-, and CoN_4C all exhibit modest or favorable thermodynamics for *CO formation, but are inhibited by large energetic penalties for CO desorption. At $-0.3\ V_{SHE}$, the first step of CO_2R over Cr- and MnN_4C proceeds through a PCET to immediately form *COOH as the grand free energy of the second state, $*CO_2^- + 2H_3O^+$, is +0.34 and +0.48 eV higher than that of the first and third states over CrN_4C and +0.36 and +0.41 eV higher over MnN_4C, respectively. Although the third state is nearly thermoneutral with the first one for these species at $-0.3\ V_{SHE}$, its immediate protonation to form *CO is thermodynamically favorable. At more reducing potentials, the formation of $*CO_2^-$ and *COOH become more thermodynamically accessible, further facilitating the production of *CO; however, CO desorption becomes even more prohibitive at these potentials. This behavior is consistent with experimental observations that MnN_xC produces CO more selectively at lower potentials and very sluggishly at moderate to high cathodic potentials.[12,19,51,52]

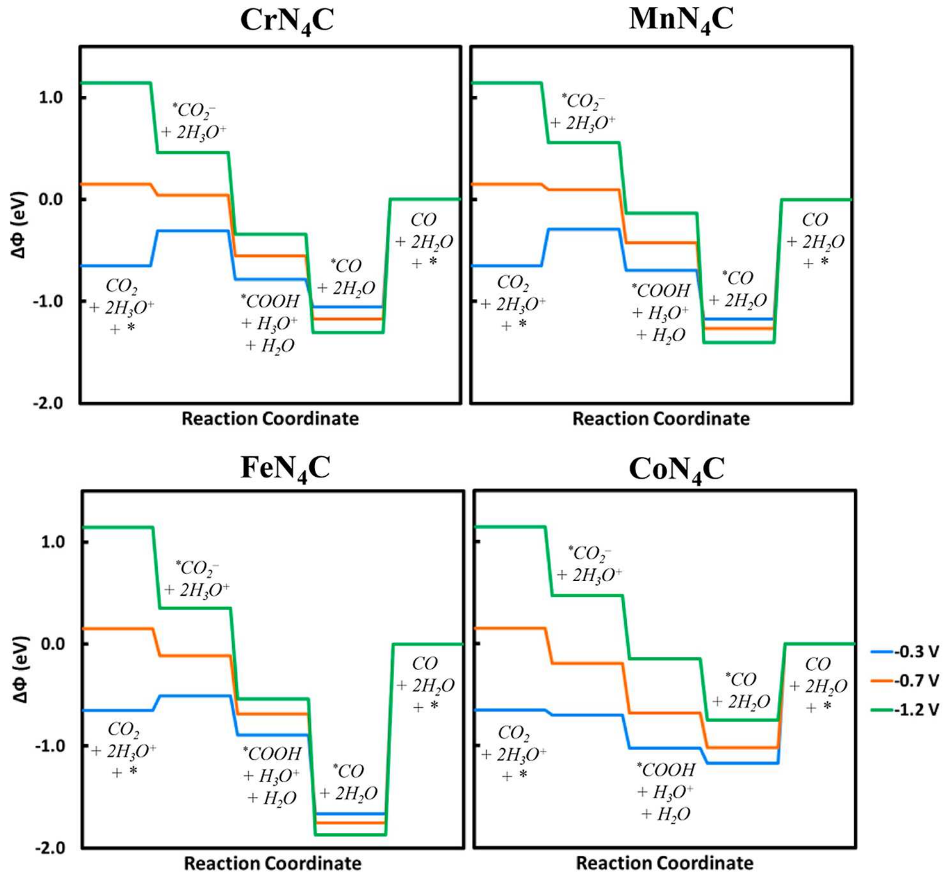

Figure 4. CO_2R reaction coordinate diagrams for Cr-, Mn-, Fe-, and CoN_4C at $\varphi = -0.3$ (blue), -0.7 (orange), and -1.2 V_{SHE} (green). FeN_4C has the potential to produce beyond CO products due to its extremely stable *CO intermediate.

CO_2R catalyzed by Fe- and CoN_4C at -0.3 V_{SHE} could proceed through either a PCET or DPET to form *COOH as the first and second states are nearly thermoneutral. Our thermodynamic analysis based on GC-DFT-computed grand free energies indicates that CO_2R on Fe- and CoN_4C via both DPET and PCET mechanisms is independent of pH, as the $*CO_2^-$ adsorption and the CO desorption steps do not require the transfer of a proton. On the other hand, a noticeable shift occurs in the reaction mechanism for all four middle MN_4Cs at more reducing potentials where $*CO_2^-$ becomes substantially more stable than $CO_{2(aq)}$ and the mechanism becomes exergonic until *CO desorption. For biases where $\varphi \geq -0.7$ V_{SHE}, CO_2 is considerably more likely to adsorb on the middle 3d MN_4Cs than to undergo hydrogenation by PCET to form *COOH, which is consistent with commonly observed behavior over homogeneous catalysts.[46,53,54] Thus, GC-DFT predicts that CO_2R activation by these catalysts is not pH-dependent under moderately cathodic conditions.

As the metal atomic number increases from Cr → Mn → Fe, *CO desorption becomes less favorable. At -1.2 $V_{SHE,}$ the *CO desorption energy, $E_{des}(CO)$, is 0.567 eV less favorable on FeN_4C than on CrN_4C. It is worth noting that the energetic differences in *CO stability calculated by GC-DFT are not equivalent to the changes in applied bias, as assumed in CHE calculations. This is because GC-DFT directly describes changes in the number of electrons of the quantum mechanically modeled portion of the electrified interface to maintain equilibrium with the Fermi level of the electron reservoir.[28]

In contrast to the aforementioned MN_4Cs, *CO becomes significantly less stable and thus desorbs more favorably on CoN_4C as more reducing potentials are applied. However, our results predict that highly endergonic *CO desorption slows or poisons CO_2R over CrN_4C, MnN_4C, and FeN_4C at all considered potentials. The large endergonicity of *CO desorption likely causes it to be the RDS of CO_2R to CO for pyridinic CrN_4C, MnN_4C, and FeN_4C, which supports experimental observations of pH-independent CO production over FeN_xC and molecular MNC analogues.[13,55] While CrN_4C is likely to exhibit less poisoning than Mn- and FeN_4C, experimental studies have found HER to outcompete CO_2R over CrN_4C, which can be partially attributed to the large barrier for CO desorption.[51] However, our results predict that highly endergonic *CO desorption poisons or slows CO_2R over Cr-, Mn-, Fe-, and CoN_4C at all considered potentials. The large endergonicity of *CO desorption likely causes it to be the RDS of CO_2R to CO for pyridinic CrN_4C, MnN_4C, and FeN_4C, which supports experimental observations of pH-independent CO production over FeN_xC and molecular MNC analogues.[13,55]

The exceptionally large energy required to desorb *CO from FeN_4C at all potentials considered in this study (>1.67 eV) indicates that it would remain on the surface sufficiently long to possibly undergo further conversion to hydrocarbon products. CH_4 production over FeN_xC has been observed experimentally, one of the few known catalysts outside of copper to do so, which has contributed to the intense interest in MNCs for CO_2R.[9,56] However, the size of the barrier required to desorb *CO from FeN_4C leads us to conclude that

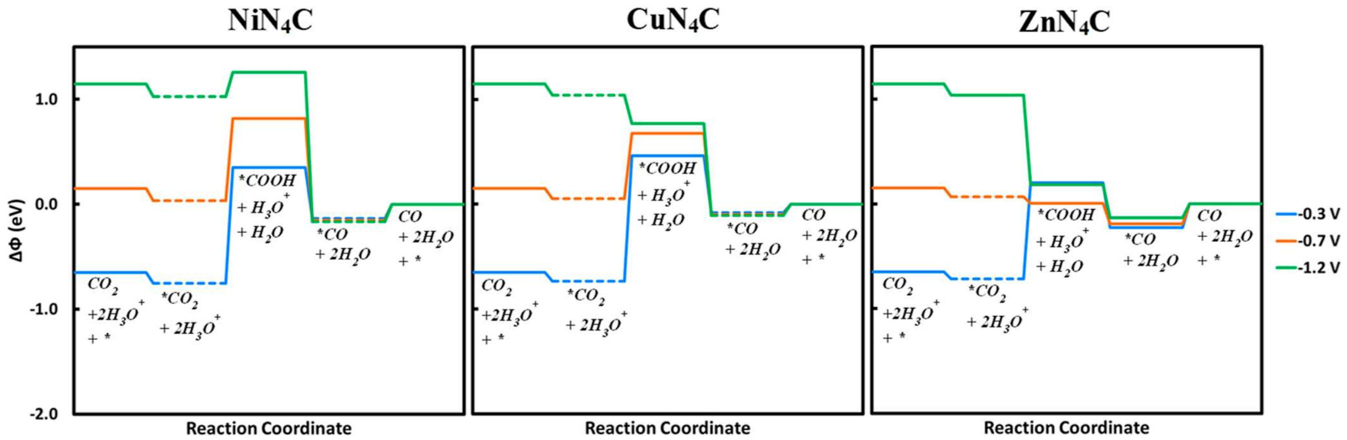

Figure 5. CO_2R reaction coordinate diagrams for Ni-, Cu-, and ZnN_4C at $\varphi = -0.3$ (blue), -0.7 (orange), and -1.2 V_{SHE} (green). Physisorbed molecules are indicated by a dashed line. Note that Ni- and CuN_4C do not chemisorb CO_2 and CO at any considered bias.

pyridinic FeN_4C is likely not the most active FeN_xC motif. A recent study on FeN_xC suggested that the axial coordination of a pyrrolic N ligand to the FeN_4C motif reduces the electron density over the metal center, which decreases the π-backdonation to CO_2 and Fe−C bond strength.[30] Similar suggestions have been offered about MnN_xC catalysts,[19,51] and GC-DFT modeling of CO_2R over MnN_xC and FeN_xC sites with different nitrogen coordinations and functionalities can help determine the nature of the MNC active site responsible for CO_2R on Mn- and Fe-based MNCs.[52]

For the case of CoN_4C, GC-DFT predicts that the formation of all intermediates at all biases is exergonic relative to the reactants such that CO_2R is thermodynamically accessible at all applied potentials considered, although it is most favored at -1.2 V_{SHE} due to the lowered $E_{des}(CO)$. This agrees with experimental studies;[51,55] however, both studies reported intense HER competition with CO_2R over synthesized CoN_xC that was not observed for cobalt-based molecular electrocatalysts.[57−60] Discrete CoN_xC catalysts have a different coordination sphere that involves pyrrolic nitrogen atoms that affect the electronic density on the Co center, possibly suppressing HER. Therefore, future computational studies that examine the effect of nitrogen coordination may elucidate the mechanism of HER suppression over CoN_xC.

CO_2R on Late 3d Metal MN_4Cs. The most notable difference between the late and middle MN_4Cs is the significantly decreased barrier for *CO desorption. Experimental studies have reported that both Ni- and ZnN_4C are highly selective for CO, which is supported by $E_{des}(CO)$ being no larger than 0.23 eV. This diminished barrier implies that *CO and $CO_{(aq)}$ coexist in equilibrium, as shown previously.[61]

Similar to FeN_xC, NiN_xC has also generated considerable interest among researchers studying MNC materials. Due to the fact that GC-DFT predicts that $CO_{2(aq)}$ only physisorbs at the NiN_4C surface, it is expected that *COOH must be formed through a PCET over NiN_4C at all potentials. However, as shown in Figure 5, the high energies of the *COOH intermediate relative to $CO_{2(aq)}$ on NiN_xC predict that CO_2R over NiN_4C is not thermodynamically favored at potentials less reducing than -0.7 V_{SHE}. At -0.7 V_{SHE}, the formation of *COOH is still slightly higher in energy than $CO_{2(aq)}$, so the reaction is expected to be kinetically slow and dependent upon available proton donors. Furthermore, the presence of hydrogen bonding has been shown to stabilize CO_2R intermediates on NiN_xC.[65] We found that including one explicit H_2O molecule oriented toward the hydrogen atom of *COOH moderately stabilizes *COOH, but that this effect diminishes at more reducing potentials (see Supporting Information, Figure S10). As shown in Supporting Information, Figure S10, at -0.7 V_{SHE}, the energy of *COOH on NiN_4C is 0.31 eV lower when an explicit H_2O H-bonded to *COOH is added to the model. This makes the overall pathway appear to lie within the limits of our thermodynamic criterion of 0.7 eV. However, in the same paper,[65] the authors found that the kinetic barrier for the formation of *COOH (including H-bonding) is >1 eV and as such, the NiN_4C site is unlikely to be sufficiently active at 298 K for CO_2R to proceed at an appreciable rate at the considered potentials.

These results contradict previous DFT studies that argued that NiN_4C is the most active and selective site for CO_2R to CO of a synthesized NiN_xC catalyst at moderate potentials.[15,31,62] However, our results join a growing number of studies that question whether pyridinic NiN_4C is the most active site for CO_2R at moderate potentials as recent studies have reported increased stabilization of the *COOH intermediate as the number of coordinating nitrogen atoms is reduced.[18,48,63−65] Hossain et al.[63] applied a grand canonical approach to study the kinetics of CO_2R on pyridinic NiN_2C, NiN_3C, and NiN_4C, in which they conclude that the NiN_4C site is highly selective toward CO only at potentials more negative than -1.4 V_{SHE}, which is consistent with the results reported herein. In contrast, they predict that NiN_2C is highly selective at potentials between -1.1 and -1.3 V_{SHE}. In an ab initio molecular dynamics simulation that included hydrogen bonding and explicit surface charge, NiNC was found to be the most active and selective Ni-based MNC for CO_2R at -0.65 V_{RHE}.[66] The rationale given for NiNC's superior performance was that its optimal charge capacity of an excess of two electrons at the studied potential facilitated electrochemical steps without increasing the bond strength of *CO so much as to prevent its desorption. Experimental electrochemical studies of CO_2R on NiN_xC show that CO is produced at potentials ranging from -0.6 to -1.6 V_{SHE}, with the maximum FE of CO lying between -0.9 and -1.3 V_{SHE}.[14,15,62] These observations and our calculations, which show that *COOH lies prohibitively high in energy, led us to conclude that NiN_4C is not the active site responsible for CO production at less reducing potentials and that NiN_xC sites with $x \leq 3$ are likely responsible for NiN$_x$C's activation of CO$_2$R to CO with high selectivities, especially at practical potentials that are most relevant to industrial applications (i.e., operating potentials less negative than -1.0 V$_{SHE}$).

While bulk metallic copper is arguably the most studied catalyst for CO$_2$R, CuN$_4$C has been studied comparatively less. Our results, shown in Figure 5, predict that CO$_2$R over CuN$_4$C is thermodynamically accessible except at -0.3 V$_{SHE}$, where the thermodynamic barrier for $^*CO_2^- \rightarrow {}^*COOH$ of 1.2 eV is too large to meet our criterion to be consistent with a reasonable reaction rate. Prior experimental work has shown that CuN$_x$C reduces CO$_2$ to CO,[12] albeit with low selectivities. However, the authors found evidence that CuN$_x$C is not stable and may form Cu nanoparticles that could activate the observed conversion of CO$_2$ into CO and other hydrocarbons. If clean CuN$_4$C is successfully synthesized, our GC-DFT results predict that it involves minimal thermodynamic barriers to catalyze CO$_2$R at ambient temperatures.

Although the stability of the ZnN$_4$C complex has been questioned,[2] recent experiments demonstrated that it is a highly active, selective, and robust catalyst for CO$_2$R to CO. Chen et al.[11] and Yang et al.[10] reported 91 and 95% FE of CO on ZnN$_x$C with maximum FE and CO partial current densities attained at potentials of approximately -0.9 and -1.2 V$_{SHE}$, respectively. Our GC-DFT results predict that for CO$_2$R on ZnN$_4$C at -0.3 and -0.7 V$_{SHE}$, $^*CO_2^-$ is unable to chemisorb and CO$_2$R instead proceeds via PCET. At -0.7 V$_{SHE}$, the reaction steps are nearly thermoneutral from reactants to products, but become exergonic at the highly reducing potential of -1.2 V$_{SHE}$ with the exception of *CO desorption, which is largely invariant to potential and slightly endergonic.

The results discussed above demonstrate the power of GC-DFT for modeling processes at electrified interfaces relative to conventional DFT methods that fix the electron number. For example, GC-DFT clearly shows that a more reducing voltage does not always stabilize adsorbates. In some cases, such as $^*CO_2^-$ adsorbed to all MN$_4$Cs, reducing potentials are entirely stabilizing (more favorable adsorption energies), whereas in others, such as *CO on FeN$_4$C, they are destabilizing. In all cases, the effects are unique to both the MNC metal and adsorbate identities. Furthermore, in contrast to the CHE model, directly computing the grand free energies at different biases using GC-DFT shows that the energies generally do not change proportionally to the applied potential. Large differences in explicit-bias effects between some 2D-materials and 3-dimensional metal catalysts were demonstrated by Kim et al.[66] They found that the chemical reactivity of 2D materials could be considerably more sensitive to applied potential than a Pt bulk metal catalyst, summarily calling into question mechanisms predicted over 2D materials by charge neutral DFT. By comparing the change in the electronic density of states, the authors concluded that the differences arose from the much smaller quantum capacitance of 2D materials, which resulted in comparatively smaller changes in electron number required to occupy or vacate the electronic bands to shift the Fermi level to match the applied potential.

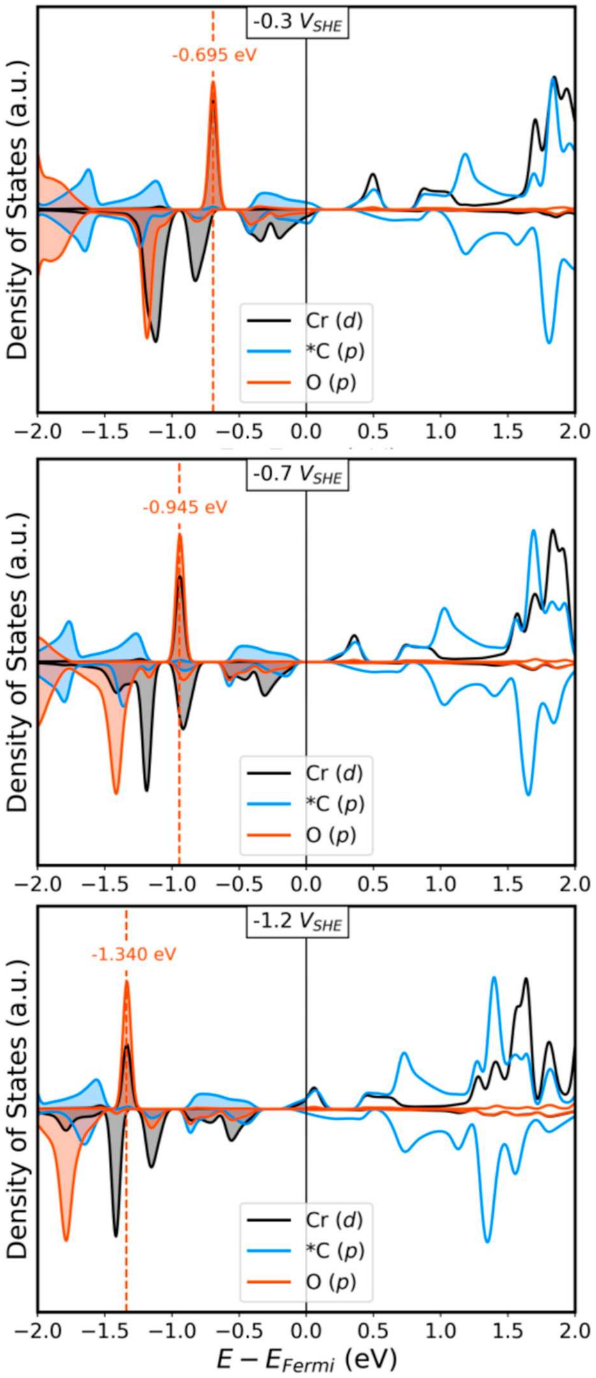

Figure 6. PDOS plots of $^*CO_2^-$ over CrN$_4$C at $\varphi = -0.3$, -0.7, and -1.2 V$_{SHE}$. Only the chromium d-states (black), carbon p-states (blue), and oxygen p-states (orange) are included here. The dashed orange line tracks the $^*CO_2^-$ π^* states. All states have been scaled to their highest respective peak values. Note the non-linear shifts and the changing shapes of the states as the applied potential shifts to more cathodic values.

The potential causes non-linear effects not only on grand free energies but also on the projected density of states (PDOS) where the shifts of the energies of the electronic states (electronic orbitals) differ from those predicted by the rigid band model (RBM), such as the CHE approximation. In contrast, a RBM predicts linear stabilizing shifts based on the number of transferred electrons for cathodic reactions. Figure 6 shows the non-linear change in the PDOS computed using GC-DFT for $^*CO_2^-$ on CrN$_4$C as a function of potential. For instance, the overlapping O 2p and Cr 3d peaks, initially at -0.695 eV for the -0.3 V$_{SHE}$ case, shift together by 0.25 eV to lower energies relative to the Fermi level, whereas the spin-down Cr 3d peak at -0.820 eV shift only by 0.095 eV when sweeping the applied potential from -0.3 to -0.7 V$_{SHE}$. Furthermore, the initially broad Cr 3d peak at -1.140 eV is deconvolved by the bias into 2 peaks, including a sharp Cr 3d peak, which shifts together with the spin-down Cr 3d peak that was initally at −0.820 eV, and a Cr 3d peak that shifts together with an O 2p peak, originally overlapped with the shoulder of the broad Cr 3d peak. These effects of the applied bias on both the shapes and peak positions of the PDOS predicted by GC-DFT influence the occupation of states and deviates from those predicted by RBMs, which neglect electronic interactions and assume that the Fermi level sweeps up or down through the DOS by an amount equal to that of the applied potential. Consequently, RBMs do not correctly describe the stabilization/destabilization and change in occupation of states caused by the non-linear potential effect on the PDOS nor its effect on adsorbate geometry, which also influences the degree of orbital mixing.

Table 1 details how the GC-DFT-computed $^*CO_2^-$ π^* peak energies shift within the studied potential range and how they differ from the shifts predicted by the RBM. The details of energy calculations are described in the Supporting Information. Additionally, a comparison of the projected DOS of *CO on ScN_4C and VN_4C is presented in Figure S9 of the Supporting Information to address differences of how adsorption energies are affected by applied external bias. These results suggest that future work should explore the nature of the effect of potential on the electronic structure of electrocatalysts using methods such as GC-DFT that fundamentally describe electrified interfaces.

Table 1. Grand Free Energies of the $^*CO_2$ π^* State as Computed Using GC-DFT and as Calculated Using the Rigid-Band Model[a]

applied potential (V_{SHE})	$^*CO_2^-$ π^* energy (GC-DFT, eV)	$^*CO_2^-$ π^* energy (rigid shift, eV)
−0.3	−0.695	−0.695[b]
−0.7	−0.945	−1.095[c]
−1.2	−1.340	−1.595[c]

[a]Energies are referenced to their respective Fermi energies at each applied potential. The CHE approximation is applied from the reference energy of the $^*CO_2$ π^* state at $\varphi = -0.3$ V_{SHE}, which is −0.63 eV. [b]This value is computed using GC-DFT at −0.3 V_{SHE} and is expected to be different when computed using conventional DFT methods. [c]Shifted values from the $^*CO_2^-$ π^* energy at $\varphi = -0.3$ V_{SHE} depending on the number of transferred electrons.

■ CONCLUSIONS

We applied GC-DFT to investigate the effects of applied potential on the CO_2R energetics and electronic structures of the 10 3d-block transition metal MN_4Cs at applied potentials of −0.3, −0.7, and −1.2 V_{SHE}. GC-DFT computed reaction coordinate diagrams exhibit a high sensitivity of the $^*CO_2^-$ adsorption grand free energy to potential for all MN_4Cs, indicating that the stability of the $^*CO_2^-$ intermediate is crucial for activating the CO_2R pathway. PDOS plots suggest that metal d-orbital and CO_2 electronic states shift nonlinearly with increasingly reducing applied potentials. This observation provides new fundamental insights into the effects of applied potential on the electronic structure of electrocatalysts. Of the pyridinic MN_4Cs examined, GC-DFT predicts that Sc-, Ti-, Co-, Cu-, and ZnN_4C are active for electrocatalytic CO_2R to CO at moderate to highly reducing potentials (i.e., $\varphi = -0.7$ to −1.2 V_{SHE}). Pyridinic ZnN_4C, specifically, is predicted to possess highly favorable CO_2R thermodynamics at both low and moderate reducing biases, suggesting that it is a particularly promising candidate for CO_2R to CO. GC-DFT also predicts that CO_2R over CoN_4C is pH-independent at all potentials, which is analogous to the behavior of the molecular cobalt protoporphyrin catalyst. For the cases of pyridinic Cr-, Mn-, and FeN_4C, the rate of CO_2R is predicted to be limited by the prohibitively large grand free energy to desorb CO. This prediction is consistent with prior experimental observations for CO_2R on FeN_xC where the CO formation rate was observed to be pH independent at more negative biases, as the rate limiting CO desorption step does not require the presence of protons.

We suggest that future computational studies investigating CO_2R catalyzed electrochemically by MN_xCs focus on examining the RDS, the dependence of transition state energies to the applied potential, and the effects of N functionality and coordination on the reactivity. The utility of GC-DFT as a computational tool is exemplified by its exceptional ability to predict potential dependent properties and, in contrast to the CHE approach, to distinguish between steps that do not involve proton transfers at varying biases. GC-DFT's broad applicability, more sound fundamental basis, and few limiting assumptions suggest that it is an appropriate method for describing processes at electrified interfaces and thus opens a new horizon for computational electrochemical modeling.

■ ASSOCIATED CONTENT

Supporting Information

The Supporting Information is available free of charge at https://pubs.acs.org/doi/10.1021/acscatal.2c01832.

Rigid shift (CHE) calculation details, additional MN_xC configurations, solvation details, GC-DFT details, energy calculations, CO_2 adsorption geometries on MnN_4C, bond lengths and angles, comparison of CHE to GC-DFT, PDOS plots of *CO on ScN_4C and VN_4C, and effect of hydrogen bonding on $^*COOH\text{-}NiN_4C$ (PDF)

■ AUTHOR INFORMATION

Corresponding Authors

Abdulaziz W. Alherz − *Department of Chemical and Biological Engineering, University of Colorado Boulder, Boulder, Colorado 80309, United States; Department of Chemical Engineering, College of Engineering and Petroleum, Kuwait University, Safat 13060, Kuwait;* orcid.org/0000-0001-7529-3483; Email: abdulaziz.alherz@colorado.edu

Charles B. Musgrave − *Department of Chemical and Biological Engineering, Renewable and Sustainable Energy Institute, and Materials Science and Engineering Program, University of Colorado Boulder, Boulder, Colorado 80309, United States;* orcid.org/0000-0002-5732-3180; Email: charles.musgrave@colorado.edu

Authors

Paige Brimley − *Department of Chemical and Biological Engineering, University of Colorado Boulder, Boulder, Colorado 80309, United States;* orcid.org/0000-0002-9064-922X

Hussain Almajed − *Department of Chemical and Biological Engineering, University of Colorado Boulder, Boulder, Colorado 80309, United States;* orcid.org/0000-0003-3604-5932

Yousef Alsunni − *Department of Chemical and Biological Engineering, University of Colorado Boulder, Boulder, Colorado 80309, United States; Chemical Engineering Department, King Fahd University of Petroleum and Minerals, Dhahran 31261, Saudi Arabia;* orcid.org/0000-0002-2417-8482

Zachary J. L. Bare − *Department of Chemical and Biological Engineering, University of Colorado Boulder, Boulder, Colorado 80309, United States*

Wilson A. Smith − *Department of Chemical and Biological Engineering and Renewable and Sustainable Energy Institute, University of Colorado Boulder, Boulder, Colorado 80309, United States; National Renewable Energy Laboratory, Golden, Colorado 80401, United States; Materials for Energy Conversion and Storage (MECS), Department of Chemical Engineering, Faculty of Applied Sciences, Delft University of Technology, Delft 2629 HZ, The Netherlands;* orcid.org/0000-0001-7757-5281

Complete contact information is available at:
https://pubs.acs.org/10.1021/acscatal.2c01832

Author Contributions

$^{\nabla}$P.B. and H.A. contributed equally. All authors have given approval to the final version of the manuscript.

Funding

CBM acknowledges support from the National Science Foundation (CBET-2016225) and from the U.S. Department of Energy, Office of Science, Basic Energy Sciences, under Award #DE-SC0022247. H.A. acknowledges support from the Saudi Ministry of Education under the King Abdullah Scholarship Program sponsored by the Saudi Arabian Cultural Mission in the United States. A.H. acknowledges support from Kuwait University. P.B. acknowledges support from a U.S. Department of Education Graduate Assistance in Areas of National Need Fellowship. This work utilized resources from the University of Colorado Boulder Research Computing Group, which is supported by the National Science Foundation (awards ACI-1532235 and ACI-1532236), the University of Colorado Boulder, and Colorado State University.

Notes

The authors declare no competing financial interest.

REFERENCES

(1) Whipple, D. T.; Kenis, P. J. A. Prospects of CO2 Utilization via Direct Heterogeneous Electrochemical Reduction. *J. Phys. Chem. Lett.* **2010**, *1*, 3451−3458.

(2) Varela, A. S.; Ju, W.; Bagger, A.; Franco, P.; Rossmeisl, J.; Strasser, P. Electrochemical Reduction of CO2 on Metal-Nitrogen-Doped Carbon Catalysts. *ACS Catal.* **2019**, *9*, 7270−7284.

(3) Kuhl, K. P.; Hatsukade, T.; Cave, E. R.; Abram, D. N.; Kibsgaard, J.; Jaramillo, T. F. Electrocatalytic Conversion of Carbon Dioxide to Methane and Methanol on Transition Metal Surfaces. *J. Am. Chem. Soc.* **2014**, *136*, 14107−14113.

(4) Lu, Q.; Rosen, J.; Zhou, Y.; Hutchings, G. S.; Kimmel, Y. C.; Chen, J. G.; Jiao, F. A Selective and Efficient Electrocatalyst for Carbon Dioxide Reduction. *Nat. Commun.* **2014**, *5*, 3242.

(5) Vesborg, P. C. K.; Jaramillo, T. F. Addressing the Terawatt Challenge: Scalability in the Supply of Chemical Elements for Renewable Energy. *RSC Adv.* **2012**, *2*, 7933−7947.

(6) Hori, Y.; Wakebe, H. H. I.; Tsukamoto, T.; Koga, O. Electrocatalytic Process of CO Selectivity in Electrochemical Reduction of CO2 at Metal Electrodes in Aqueous Media. *Electrochim. Acta* **1994**, *39*, 1833−1839.

(7) Tripkovic, V.; Vanin, M.; Karamad, M.; Björketun, M. E.; Jacobsen, K. W.; Thygesen, K. S.; Rossmeisl, J. Electrochemical CO2 and CO Reduction on Metal-Functionalized Porphyrin-like Graphene. *J. Phys. Chem. C* **2013**, *117*, 9187−9195.

(8) Barona-Castaño, J. C.; Carmona-Vargas, C. C.; Brocksom, T. J.; de Oliveira, K. T.; Graça, M.; Neves, P. M. S.; Amparo, M.; Faustino, F. Porphyrins as Catalysts in Scalable Organic Reactions. *Molecules* **2016**, *21*, 310.

(9) Ju, W.; Bagger, A.; Wang, X.; Tsai, Y.; Luo, F.; Möller, T.; Wang, H.; Rossmeisl, J.; Varela, A. S.; Strasser, P. Unraveling Mechanistic Reaction Pathways of the Electrochemical CO2 Reduction on Fe-N-C Single-Site Catalysts. *ACS Energy Lett.* **2019**, *4*, 1663−1671.

(10) Yang, F.; Song, P.; Liu, X.; Mei, B.; Xing, W.; Jiang, Z.; Gu, L.; Xu, W. Highly Efficient CO2 Electroreduction on ZnN4-Based Single-Atom Catalyst. *Angew. Chem., Int. Ed.* **2018**, *57*, 12303−12307.

(11) Chen, Z.; Mou, K.; Yao, S.; Liu, L. Zinc-Coordinated Nitrogen-Codoped Graphene as an Efficient Catalyst for Selective Electrochemical Reduction of CO2 to CO. *ChemSusChem* **2018**, *11*, 2944−2952.

(12) Li, J.; Pršlja, P.; Shinagawa, T.; Martín Fernández, A. J.; Krumeich, F.; Artyushkova, K.; Atanassov, P.; Zitolo, A.; Zhou, Y.; García-Muelas, R.; López, N.; Pérez-Ramírez, J.; Jaouen, F. Volcano Trend in Electrocatalytic Co2 Reduction Activity over Atomically Dispersed Metal Sites on Nitrogen-Doped Carbon. *ACS Catal.* **2019**, *9*, 10426−10439.

(13) Varela, A. S.; Kroschel, M.; Leonard, N. D.; Ju, W.; Steinberg, J.; Bagger, A.; Rossmeisl, J.; Strasser, P. PH Effects on the Selectivity of the Electrocatalytic CO2 Reduction on Graphene-Embedded Fe-N-C Motifs: Bridging Concepts between Molecular Homogeneous and Solid-State Heterogeneous Catalysis. *ACS Energy Lett.* **2018**, *3*, 812−817.

(14) Möller, T.; Ju, W.; Bagger, A.; Wang, X.; Luo, F.; Ngo Thanh, T.; Varela, A.; Rossmeisl, J.; Strasser, P. Efficient CO 2 to CO Electrolysis on Solid Ni-N-C Catalysts at Industrial Current Densities†. *Energy Environ. Sci.* **2019**, *12*, 640.

(15) Yang, H. B.; Hung, S. F.; Liu, S.; Yuan, K.; Miao, S.; Zhang, L.; Huang, X.; Wang, H. Y.; Cai, W.; Chen, R.; Gao, J.; Yang, X.; Chen, W.; Huang, Y.; Chen, H. M.; Li, C. M.; Zhang, T.; Liu, B. Atomically Dispersed Ni(i) as the Active Site for Electrochemical CO2 Reduction. *Nat. Energy* **2018**, *3*, 140−147.

(16) Lu, P.; Yang, Y.; Yao, J.; Wang, M.; Dipazir, S.; Yuan, M.; Zhang, J.; Wang, X.; Xie, Z.; Zhang, G. Facile Synthesis of Single-Nickel-Atomic Dispersed N-Doped Carbon Framework for Efficient Electrochemical CO2 Reduction. *Appl. Catal., B* **2019**, *241*, 113−119.

(17) Su, P.; Iwase, K.; Nakanishi, S.; Hashimoto, K.; Kamiya, K. Nickel-Nitrogen-Modified Graphene: An Efficient Electrocatalyst for the Reduction of Carbon Dioxide to Carbon Monoxide. *Small* **2016**, *12*, 6083−6089.

(18) Yan, C.; Li, H.; Ye, Y.; Wu, H.; Cai, F.; Si, R.; Xiao, J.; Miao, S.; Xie, S.; Yang, F.; Li, Y.; Wang, G.; Bao, X. Coordinatively Unsaturated Nickel-Nitrogen Sites towards Selective and High-Rate CO2 Electroreduction. *Energy Environ. Sci.* **2018**, *11*, 1204−1210.

(19) Feng, J.; Gao, H.; Zheng, L.; Chen, Z.; Zeng, S.; Jiang, C.; Dong, H.; Liu, L.; Zhang, S.; Zhang, X. A Mn-N3 Single-Atom Catalyst Embedded in Graphitic Carbon Nitride for Efficient CO2 Electroreduction. *Nat. Commun.* **2020**, *11*, 4341.

(20) Zhang, C.; Fu, Z.; Zhao, Q.; Du, Z.; Zhang, R.; Li, S. Single-Atom-Ni-Decorated, Nitrogen-Doped Carbon Layers for Efficient Electrocatalytic CO2 Reduction Reaction. *Electrochem. Commun.* **2020**, *116*, 106758.

(21) Franco, F.; Rettenmaier, C.; Jeon, H. S.; Roldan Cuenya, B. Transition Metal-Based Catalysts for the Electrochemical CO 2 Reduction: From Atoms and Molecules to Nanostructured Materials. *Chem. Soc. Rev.* **2020**, *49*, 6884.

(22) Kattel, S.; Atanassov, P.; Kiefer, B. Stability, Electronic and Magnetic Properties of In-Plane Defects in Graphene: A First-Principles Study. *J. Phys. Chem. C* **2012**, *116*, 8161.

(23) Bagger, A.; Ju, W.; Varela, A. S.; Strasser, P.; Rossmeisl, J. Single Site Porphyrine-like Structures Advantages over Metals for Selective Electrochemical CO 2 Reduction. *Catal. Today* **2017**, *288*, 74−78.

(24) Varela, A. S.; Ju, W.; Strasser, P. Molecular Nitrogen−Carbon Catalysts, Solid Metal Organic Framework Catalysts, and Solid Metal/Nitrogen-Doped Carbon (MNC) Catalysts for the Electrochemical CO2 Reduction. *Adv. Energy Mater.* **2018**, *8*, 1703614.

(25) Alsunni, Y. A.; Alherz, A. W.; Musgrave, C. B. Electrocatalytic Reduction of CO2 to CO Over Ag(110) and Cu(211) Modeled by Grand Canonical Density Functional Theory. *J. Phys. Chem. C* **2021**, *125*, 23773.

(26) Nørskov, J. K.; Rossmeisl, J.; Logadottir, A.; Lindqvist, L.; Kitchin, J. R.; Bligaard, T.; Jónsson, H. Origin of the Overpotential for Oxygen Reduction at a Fuel-Cell Cathode. *J. Phys. Chem. B* **2004**, *108*, 17886−17892.

(27) Sundararaman, R.; Letchworth-Weaver, K.; Schwarz, K. A.; Gunceler, D.; Ozhabes, Y.; Arias, T. A. JDFTx: Software for Joint Density-Functional Theory. *SoftwareX* **2017**, *6*, 278−284.

(28) Sundararaman, R.; Goddard, W. A.; Arias, T. A. Grand Canonical Electronic Density-Functional Theory: Algorithms and Applications to Electrochemistry. *J. Chem. Phys.* **2017**, *146*, 114104.

(29) Schwarz, K.; Sundararaman, R. The Electrochemical Interface in First-Principles Calculations. *Surf. Sci. Rep.* **2020**, *75*, 100492.

(30) Zhang, H.; Li, J.; Xi, S.; Du, Y.; Hai, X.; Wang, J.; Xu, H.; Wu, G.; Zhang, J.; Lu, J.; Wang, J. A Graphene-Supported Single-Atom FeN5 Catalytic Site for Efficient Electrochemical CO2 Reduction. *Angew. Chem., Int. Ed.* **2019**, *58*, 14871−14876.

(31) Li, X.; Bi, W.; Chen, M.; Sun, Y.; Ju, H.; Yan, W.; Zhu, J.; Wu, X.; Chu, W.; Wu, C.; Xie, Y. Exclusive Ni-N4 Sites Realize Near-Unity CO Selectivity for Electrochemical CO2 Reduction. *J. Am. Chem. Soc.* **2017**, *139*, 14889−14892.

(32) Liu, T.; Wang, Q.; Wang, G.; Bao, X. Electrochemical CO2reduction on Graphdiyne: A DFT Study. *Green Chem.* **2021**, *23*, 1212−1219.

(33) Gong, L.; Zhang, D.; Lin, C. Y.; Zhu, Y.; Shen, Y.; Zhang, J.; Han, X.; Zhang, L.; Xia, Z. Catalytic Mechanisms and Design Principles for Single-Atom Catalysts in Highly Efficient CO2 Conversion. *Adv. Energy Mater.* **2019**, *9*, 201902625.

(34) Peterson, A. A.; Abild-Pedersen, F.; Studt, F.; Rossmeisl, J.; Nørskov, J. K. How Copper Catalyzes the Electroreduction of Carbon Dioxide into Hydrocarbon Fuels. *Energy Environ. Sci.* **2010**, *3*, 1311−1315.

(35) Liu, H.; Liu, J.; Yang, B. Modeling the Effect of Surface CO Coverage on the Electrocatalytic Reduction of CO2 to CO on Pd Surfaces. *Phys. Chem. Chem. Phys.* **2019**, *21*, 9876−9882.

(36) Gauthier, J. A.; Dickens, C. F.; Heenen, H. H.; Vijay, S.; Ringe, S.; Chan, K. Unified Approach to Implicit and Explicit Solvent Simulations of Electrochemical Reaction Energetics. *J. Chem. Theory Comput.* **2019**, *15*, 6895−6906.

(37) Vijay, S.; Gauthier, J. A.; Heenen, H. H.; Bukas, V. J.; Kristoffersen, H. H.; Chan, K. Dipole-Field Interactions Determine the CO 2 Reduction Activity of 2D Fe−N−C Single-Atom Catalysts. *ACS Cent. Sci.* **2020**, *10*, 7826.

(38) Akhade, S. A.; Luo, W.; Nie, X.; Asthagiri, A.; Janik, M. J. Theoretical Insight on Reactivity Trends in CO2 Electroreduction across Transition Metals. *Catal. Sci. Technol.* **2016**, *6*, 1042−1053.

(39) Han, L.; Song, S.; Liu, M.; Yao, S.; Liang, Z.; Cheng, H.; Ren, Z.; Liu, W.; Lin, R.; Qi, G.; Liu, X.; Wu, Q.; Luo, J.; Xin, H. L.; Liu, X.; Wu, Q.; Luo, J.; Xin, H. L. Stable and Efficient Single-Atom Zn Catalyst for CO2Reduction to CH4. *J. Am. Chem. Soc.* **2020**, *142*, 12563−12567.

(40) Sundararaman, R.; Goddard, W. A. The Charge-Asymmetric Nonlocally Determined Local-Electric (CANDLE) Solvation Model. *J. Chem. Phys.* **2015**, *142*, 064107.

(41) Perdew, J. P.; Burke, K.; Ernzerhof, M. Generalized Gradient Approximation Made Simple. *Phys. Rev. Lett.* **1996**, *77*, 3865−3868.

(42) Grimme, S.; Antony, J.; Ehrlich, S.; Krieg, H. A Consistent and Accurate Ab Initio Parametrization of Density Functional Dispersion Correction (DFT-D) for the 94 Elements H-Pu. *J. Chem. Phys.* **2010**, *132*, 154104.

(43) Ringe, S.; Clark, E. L.; Resasco, J.; Walton, A.; Seger, B.; Bell, A. T.; Chan, K. Understanding Cation Effects in Electrochemical CO2 Reduction. *Energy Environ. Sci.* **2019**, *12*, 3001−3014.

(44) Thorson, M. R.; Siil, K. I.; Kenis, P. J. A. Effect of Cations on the Electrochemical Conversion of CO 2 to CO. *J. Electrochem. Soc.* **2013**, *160*, F69−F74.

(45) Murata, A.; Hori, Y. Product Selectivity Addected by Cationic Species in Electrochemical Reduction of CO2 and CO at a Cu Electrode. *Chem. Soc. Japan* **1991**, *64*, 123−127.

(46) Shen, J.; Kolb, M. J.; Göttle, A. J.; Koper, M. T. M. DFT Study on the Mechanism of the Electrochemical Reduction of CO2 Catalyzed by Cobalt Porphyrins. *J. Phys. Chem. C* **2016**, *120*, 15714−15721.

(47) Shen, J.; Kortlever, R.; Kas, R.; Birdja, Y. Y.; Diaz-Morales, O.; Kwon, Y.; Ledezma-Yanez, I.; Schouten, K. J. P.; Mul, G.; Koper, M. T. M. Electrocatalytic Reduction of Carbon Dioxide to Carbon Monoxide and Methane at an Immobilized Cobalt Protoporphyrin. *Nat. Commun.* **2015**, *6*, 8177.

(48) Jiang, K.; Siahrostami, S.; Akey, A. J.; Li, Y.; Lu, Z.; Lattimer, J.; Hu, Y.; Stokes, C.; Gangishetty, M.; Chen, G.; Zhou, Y.; Hill, W.; Cai, W. B.; Bell, D.; Chan, K.; Nørskov, J. K.; Cui, Y.; Wang, H. Transition-Metal Single Atoms in a Graphene Shell as Active Centers for Highly Efficient Artificial Photosynthesis. *Chem* **2017**, *3*, 950−960.

(49) Siahrostami, S.; Jiang, K.; Karamad, M.; Chan, K.; Wang, H.; Nørskov, J. Theoretical Investigations into Defected Graphene for Electrochemical Reduction of CO2. *ACS Sustain. Chem. Eng.* **2017**, *5*, 11080−11085.

(50) Li, F.; Ai, H.; Shi, C.; Lo, K. H.; Pan, H. Single Transition Metal Atom Catalysts on Ti2CN2 for Efficient CO2 Reduction Reaction. *Int. J. Hydrogen Energy* **2021**, *46*, 12886−12896.

(51) Pan, F.; Deng, W.; Justiniano, C.; Li, Y. Identification of Champion Transition Metals Centers in Metal and Nitrogen-Codoped Carbon Catalysts for CO2 Reduction. *Appl. Catal., B* **2018**, *226*, 463−472.

(52) Zhang, B.; Zhang, J.; Shi, J.; Tan, D.; Liu, L.; Zhang, F.; Lu, C.; Su, Z.; Tan, X.; Cheng, X.; Han, B.; Zheng, L.; Zhang, J. Manganese Acting as a High-Performance Heterogeneous Electrocatalyst in Carbon Dioxide Reduction. *Nat. Commun.* **2019**, *10*, 2980.

(53) Nielsen, I. M. B.; Leung, K. Cobalt-Porphyrin Catalyzed Electrochemical Reduction of Carbon Dioxide in Water. 1. A Density Functional Study of Intermediates. *J. Phys. Chem. A* **2010**, *114*, 10166−10173.

(54) Göttle, A. J.; Koper, M. T. M. Proton-Coupled Electron Transfer in the Electrocatalysis of CO2 Reduction: Prediction of Sequential vs. Concerted Pathways Using DFT. *Chem. Sci.* **2016**, *8*, 458−465.

(55) Ju, W.; Bagger, A.; Hao, G.-P.; Varela, A. S.; Sinev, I.; Bon, V.; Cuenya, B. R.; Kaskel, S.; Rossmeisl, J.; Strasser, P. Understanding Activity and Selectivity of Metal-Nitrogen-Doped Carbon Catalysts for Electrochemical Reduction of CO2. *Nat. Commun.* **2017**, *8*, 944.

(56) Varela, A. S.; Sahraie, N. R.; Steinberg, J.; Ju, W.; Oh, H. S.; Strasser, P. Metal-Doped Nitrogenated Carbon as an Efficient Catalyst for Direct CO2 Electroreduction to CO and Hydrocarbons. *Angew. Chem., Int. Ed.* **2015**, *54*, 10758−10762.

(57) Zhang, X.; Wu, Z.; Zhang, X.; Li, L.; Li, Y.; Xu, H.; Li, X.; Yu, X.; Zhang, Z.; Liang, Y.; Wang, H. Highly Selective and Active CO2 Reduction Electrocatalysts Based on Cobalt Phthalocyanine/Carbon Nanotube Hybrid Structures. *Nat. Commun.* **2017**, *8*, 14675.

(58) Lu, X.; Wu, Y.; Yuan, X.; Huang, L.; Wu, Z.; Xuan, J.; Wang, Y.; Wang, H. High-Performance Electrochemical CO2 Reduction Cells Based on Non-Noble Metal Catalysts. *ACS Energy Lett.* **2018**, *3*, 2527−2532.

(59) Morlanés, N.; Takanabe, K.; Rodionov, V. Simultaneous Reduction of CO2 and Splitting of H2O by a Single Immobilized Cobalt Phthalocyanine Electrocatalyst. *ACS Catal.* **2016**, *6*, 3092−3095.

(60) Wang, M.; Torbensen, K.; Salvatore, D.; Ren, S.; Joulié, D.; Dumoulin, F.; Mendoza, D.; Lassalle-kaiser, B.; Umit, I.; Berlinguette, C. P.; Robert, M. CO2 Electrochemical Catalytic Reduction with a Highly Active Cobalt Phthalocyanine. *Nat. Commun.* **2019**, *10*, 3602.

(61) Zhang, Q.; Mamtani, K.; Jain, D.; Ozkan, U.; Asthagiri, A. CO Poisoning Effects on FeNC and CNx ORR Catalysts: A Combined Experimental-Computational Study. *J. Phys. Chem. C* **2016**, *120*, 15173−15184.

(62) Yang, H.; Lin, Q.; Zhang, C.; Yu, X.; Cheng, Z.; Li, G.; Hu, Q.; Ren, X.; Zhang, Q.; Liu, J.; He, C. Carbon Dioxide Electroreduction on Single-Atom Nickel Decorated Carbon Membranes with Industry Compatible Current Densities. *Nat. Commun.* **2020**, *11*, 593.

(63) Hossain, M. D.; Huang, Y.; Yu, T. H.; Goddard, W. A., III; Luo, Z. Reaction Mechanism and Kinetics for CO 2 Reduction on Nickel Single Atom Catalysts from Quantum Mechanics. *Nat. Commun.* **2020**, *11*, 2256.

(64) Gong, Y. N.; Jiao, L.; Qian, Y.; Pan, C. Y.; Zheng, L.; Cai, X.; Liu, B.; Yu, S. H.; Jiang, H. L. Regulating the Coordination Environment of MOF-Templated Single-Atom Nickel Electrocatalysts for Boosting CO2 Reduction. *Angew. Chem., Int. Ed.* **2020**, *59*, 2705−2709.

(65) Zhao, X.; Liu, Y. Unveiling the Active Structure of Single Nickel Atom Catalysis: Critical Roles of Charge Capacity and Hydrogen Bonding. *J. Am. Chem. Soc.* **2020**, *142*, 5773.

(66) Kim, D.; Shi, J.; Liu, Y. Substantial Impact of Charge on Electrochemical Reactions of Two-Dimensional Materials. *J. Am. Chem. Soc.* **2018**, *140*, 9127−9131.